EXIT-Chart-Aided Near-Capacity Quantum Turbo Code Design

Zunaira Babar, Soon Xin Ng, *Senior Member, IEEE*, and Lajos Hanzo, *Fellow, IEEE*

***Abstract*—High detection complexity is the main impediment in future gigabit-wireless systems. However, a quantum-based detector is capable of simultaneously detecting hundreds of user signals by virtue of its inherent parallel nature. This, in turn, requires near-capacity quantum error correction codes for protecting the constituent qubits of the quantum detector against undesirable environmental decoherence. In this quest, we appropriately adapt the conventional nonbinary EXtrinsic Information Transfer (EXIT) charts for quantum turbo codes (QTCs) by exploiting the intrinsic quantum-to-classical isomorphism. The EXIT chart analysis not only allows us to dispense with the time-consuming Monte Carlo simulations but facilitates the design of near-capacity codes without resorting to the analysis of their distance spectra as well. We have demonstrated that our EXIT chart predictions are in line with the Monte Carlo simulation results. We have also optimized the entanglement-assisted QTC using EXIT charts, which outperforms the existing distance-spectra-based QTCs. More explicitly, the performance of our optimized QTC is as close as 0.3 dB to the corresponding hashing bound.**

***Index Terms*—EXtrinsic Information Transfer (EXIT) charts, near-capacity design, quantum error correction, turbo codes.**

I. INTRODUCTION

MULTIUSER multiple-input multiple-output (MU-MIMO) [1], [2] and massive MIMO [3] schemes are promising candidates for the future-generation gigabit-wireless system. However, the corresponding detection complexity exponentially increases with the number of users and antennas, when aiming for approaching the optimum maximum-likelihood (ML) performance. An attractive solution to this exponentially escalating complexity problem is to perform the ML detection in the quantum domain, since quantum computing allows parallel evaluations of a function at a complexity cost that is equivalent to a single classical evaluation [4], [5]. However, a quantum detector requires powerful quantum error correction codes (QECCs) for stabilizing and protecting the fragile constituent quantum bits (qubits) against undesirable quantum decoherence, when they interact with the environment [4], [6]. Furthermore, quantum-based wireless transmission is capable of supporting secure data dissemination [4], [7], where any 'measurement' or "observation" by an eavesdropper will destroy the quantum entanglement, hence instantly intimating the parties concerned [4]. However, this requires powerful QECCs for the reliable transmission of qubits across the wireless communication channels. Hence, near-capacity QECCs are the vital enabling technique for future generations of wireless systems, which are both reliable and secure and yet operate at an affordable detection complexity.

Classical turbo codes operate almost arbitrarily close to the Shannon limit, which inspired researchers to achieve a comparable near-capacity performance for quantum systems [8]–[12]. In this quest, Poulin *et al.* developed the theory of quantum turbo codes (QTCs) in [8] and [9], based on the interleaved serial concatenation of quantum convolutional codes (QCCs) [13]–[16], and investigated their behavior on a quantum depolarizing channel.[1] It was found in [8] and [17] that the constituent QCCs cannot be simultaneously recursive and noncatastrophic. Since the recursive nature of the inner code is essential for ensuring an unbounded minimum distance, whereas the noncatastrophic nature is required to achieve decoding convergence, the QTCs in [8] and [9] had a bounded minimum distance. More explicitly, the design of Poulin *et al.* [8], [9] was based on nonrecursive and noncatastrophic convolutional codes. Later, Wilde and Hseih [10] extended the concept of preshared entanglement to QTCs, which facilitated the design of QTCs having an unbounded minimum distance. Wilde *et al.* also introduced the notion of *extrinsic* information to the iterative decoding of QTCs and investigated various code structures in [11].

The search for the optimal components of a QTC has been so far confined to the analysis of the constituent QCC distance spectra, followed by intensive Monte Carlo simulations for determining the convergence threshold of the resultant QTC, as detailed in [9] and [11]. While the distance spectrum dominates a turbo code's performance in the bit error rate (BER) floor region, it has a relatively insignificant impact on the convergence properties in the turbo-cliff region [18]. Therefore, having a good distance spectrum does not guarantee having a

Manuscript received December 14, 2013; revised April 22, 2014; accepted May 31, 2014. This work was supported in part by the Engineering and Physical Sciences Research Council under Grant EP/L018659/1; by the Research Councils UK under the India–UK Advanced Technology Center; by the EU under the CONCERTO project; by the European Research Council, Advanced Fellow Grant; and by the Royal Society's Wolfson Reasearch Merit Award. The review of this paper was coordinated by Prof. H. H. Nguyen.

The authors are with the School of Electronics and Computer Science, University of Southampton, Southampton SO17 1BJ, U.K. (e-mail: zb2g10@ecs.soton.ac.uk; sxn@ecs.soton.ac.uk; lh@ecs.soton.ac.uk).

Color versions of one or more of the figures in this paper are available online at http://ieeexplore.ieee.org.

Digital Object Identifier 10.1109/TVT.2014.2328638

---

[1] A quantum channel can be used for modeling imperfections in quantum hardware, namely, faults resulting from quantum decoherence and quantum gates. Furthermore, a quantum channel can also model quantum-state flips imposed by the transmission medium, including free-space wireless channels and optical fiber links, when qubits are transmitted across these media.

near-capacity performance; in fact, there is often a tradeoff between them. To circumvent this problem and to dispense with time-consuming Monte Carlo simulations, in this paper, we extend the application of EXtrinsic Information Transfer (EXIT) charts to the design of QTCs.

More explicitly, we have the following contributions.

- We have appropriately adapted the conventional nonbinary EXIT-chart-based design approach to the family of QTCs based on the underlying quantum-to-classical isomorphism. Similar to the classical codes, our EXIT chart predictions are in line with the Monte Carlo simulation results.
- We have analyzed the behavior of both an unassisted (nonrecursive) and an entanglement-assisted (recursive) inner convolutional code using EXIT charts for demonstrating that, similar to their classical counterparts, recursive inner quantum codes constitute families of QTCs having an unbounded minimum distance.
- For the sake of approaching the achievable capacity, we have optimized the constituent inner and outer components of QTC using EXIT charts. In contrast to the distance-spectra-based QTCs in [11], whose performance is within 0.9 dB of the hashing bound, our optimized QTC operates within 0.3 dB of the capacity limit. However, our intention was not to carry out an exhaustive code search over the potentially excessive parameter space but, instead, to demonstrate how our EXIT-chart-based approach may be involved for quantum codes. This new design approach is expected to stimulate further interest in the EXIT-chart-based near-capacity design of various concatenated quantum codes.

This paper is organized as follows. Section II provides a rudimentary introduction to quantum stabilizer codes (QSCs) and QTCs. We will then present our proposed EXIT-chart-based approach conceived for QTCs in Section III. Our results will be discussed in Section IV, and our conclusions are offered in Section V.

II. PRELIMINARIES

The constituent convolutional codes of a QTC belong to the class of stabilizer codes [19], which are analogous to classical linear block codes. Here, we will briefly review the basics of stabilizer codes to highlight this relationship for the benefit of readers with background in classical channel coding. This will be followed by a brief discussion on QTCs.

A. Stabilizer Codes

Qubits collapse to classical bits upon measurement [5], [6]. This prevents us from directly applying classical error correction techniques for reliable quantum transmission. QECCs circumvent this problem by observing the error syndromes without reading the actual quantum information. Hence, QSCs invoke the syndrome decoding approach of classical linear block codes for estimating the errors incurred during transmission.

Let us first recall some basic definitions [6].

Pauli Operators: The $\mathbf{I}$, $\mathbf{X}$, $\mathbf{Y}$, and $\mathbf{Z}$ Pauli operators are defined by the following matrices:

$$\mathbf{I} = \begin{pmatrix} 1 & 0 \\ 0 & 1 \end{pmatrix}, \quad \mathbf{X} = \begin{pmatrix} 0 & 1 \\ 1 & 0 \end{pmatrix}$$
$$\mathbf{Y} = \begin{pmatrix} 0 & -i \\ i & 0 \end{pmatrix}, \ \mathbf{Z} = \begin{pmatrix} 1 & 0 \\ 0 & -1 \end{pmatrix} \qquad (1)$$

where the $\mathbf{X}$, $\mathbf{Y}$, and $\mathbf{Z}$ operators anticommute with each other.

Pauli Group: A single-qubit Pauli group $\mathcal{G}_1$ consists of all the Pauli matrices of (1), together with the multiplicative factors ± 1 and $\pm i$, i.e., we have

$$\mathcal{G}_1 \equiv \{\pm\mathbf{I}, \pm i\mathbf{I}, \pm\mathbf{X}, \pm i\mathbf{X}, \pm\mathbf{Y}, \pm i\mathbf{Y}, \pm\mathbf{Z}, \pm i\mathbf{Z}\}. \qquad (2)$$

The general Pauli group $\mathcal{G}_n$ is an n-fold tensor product of $\mathcal{G}_1$.

Depolarizing Channel: The depolarizing channel characterized by probability p inflicts an n-tuple error $\mathcal{P} \in \mathcal{G}_n$ on n qubits, where the ith qubit may experience either a bit flip $(\mathbf{X})$, a phase flip $(\mathbf{Z})$, or both $(\mathbf{Y})$ with a probability of $p/3$.

An $[n, k]$ QSC, constructed over a code space $\mathcal{C}$, is defined by a set of $(n-k)$ independent commuting n-tuple Pauli operators g_i, for $1 \leq i \leq (n-k)$. The corresponding encoder then maps the information word (logical qubits) $|\psi\rangle \in \mathbb{C}^{2^k}$ onto the codeword (physical qubits) $|\overline{\psi}\rangle \in \mathbb{C}^{2^n}$, where $\mathbb{C}^d$ denotes the d-dimensional Hilbert space. More specifically, the corresponding stabilizer group $\mathcal{H}$ contains both g_i and all the products of g_i for $1 \leq i \leq (n-k)$ and forms an Abelian subgroup of $\mathcal{G}_n$. A unique feature of these operators is that they do not change the state of valid codewords, while yielding an eigenvalue of -1 for corrupted states. Consequently, the eigenvalue is -1 if the n-tuple Pauli error $\mathcal{P}$ anticommutes with the stabilizer g_i, and it is $+1$ if $\mathcal{P}$ commutes with g_i. More explicitly, we have

$$g_i|\hat{\psi}\rangle = \begin{cases} |\overline{\psi}\rangle, & g_i\mathcal{P} = \mathcal{P}g_i \\ -|\overline{\psi}\rangle, & g_i\mathcal{P} = -\mathcal{P}g_i \end{cases} \qquad (3)$$

where $\mathcal{P}$ is an n-tuple Pauli error, and $|\overline{\psi}\rangle \in \mathcal{C}$ and $|\hat{\psi}\rangle = \mathcal{P}|\overline{\psi}\rangle$ is the received codeword. The resultant ± 1 eigenvalue gives the corresponding error syndrome, which is 0 for an eigenvalue of $+1$ and 1 for an eigenvalue of -1. It must be mentioned here that Pauli errors that differ only by the stabilizer group have the same impact on all the codewords and, therefore, can be corrected by the same recovery operations. This gives quantum codes the intrinsic property of degeneracy [20].

As detailed in [21] and [22], QSCs may be characterized in terms of an equivalent binary parity-check matrix notation satisfying the commutativity constraint of stabilizers. This can be exploited for designing quantum codes with the aid of known classical codes. The $(n-k)$ stabilizers of an $[n, k]$ stabilizer code can be represented as a concatenation of a pair of $(n-k) \times n$ binary matrices $\mathbf{H}_z$ and $\mathbf{H}_x$, resulting in the binary parity-check matrix $\mathbf{H}$ as given in the following equation:

$$\mathbf{H} = [\mathbf{H}_z|\mathbf{H}_x]. \qquad (4)$$

More explicitly, each row of $\mathbf{H}$ corresponds to a stabilizer of $\mathcal{H}$, so that the ith column of $\mathbf{H}_z$ and $\mathbf{H}_x$ corresponds to the ith qubit, and a binary 1 at these locations represents a $\mathbf{Z}$

and $\mathbf{X}$ Pauli operator, respectively, in the corresponding stabilizer. Moreover, the commutativity requirement of stabilizers is transformed into the orthogonality of rows with respect to the symplectic product defined in [22], as follows:

$$\mathbf{H}_z\mathbf{H}_x^T + \mathbf{H}_x\mathbf{H}_z^T = 0. \tag{5}$$

Conversely, two classical linear codes $\mathbf{H}_z$ and $\mathbf{H}_x$ can be used to construct a QSC $\mathbf{H}$ of (4) if $\mathbf{H}_z$ and $\mathbf{H}_x$ meet the symplectic criterion of (5).

In line with this discussion, a Pauli error operator $\mathcal{P}$ can be represented by the effective error P, which is a binary vector of length $2n$. More specifically, P is a concatenation of n bits for $\mathbf{Z}$ errors, followed by another n bits for $\mathbf{X}$ errors, and the resultant syndrome is given by the symplectic product of $\mathbf{H}$ and P, which is equivalent to $\mathbf{H}[P_x : P_z]^T$. In other words, the Pauli-$\mathbf{X}$ operator is used for correcting $\mathbf{Z}$ errors, whereas the Pauli-$\mathbf{Z}$ operator is used for correcting $\mathbf{X}$ errors [6]. Thus, the quantum-domain syndrome is equivalent to the classical-domain binary syndrome, and a basic quantum-domain decoding procedure is similar to the syndrome-based decoding of the equivalent classical code [22]. However, due to the degenerate nature of quantum codes, quantum decoding aims at finding the most likely error coset, whereas classical syndrome decoding finds the most likely error.

B. QTCs

Analogous to classical serially concatenated (SC) turbo codes, QTCs are obtained from the interleaved serial concatenation of QCCs, which belong to the class of stabilizer codes. However, it is more convenient to exploit the circuit-based representation of the constituent codes, rather than the conventional parity-check-matrix-based syndrome decoding [23]. Before proceeding with the decoding algorithm, we will briefly review the circuit-based representation. This discussion is based on [9].

Let us consider an (n, k) classical linear block code constructed over the code space C, which maps the information word $c \in \mathbb{F}_2^k$ onto the corresponding codeword $\overline{c} \in \mathbb{F}_2^n$. In the circuit-based representation, code space C is defined as follows:

$$C = \{\overline{c} = (c : 0_{n-k})V\} \tag{6}$$

where V is an $(n \times n)$-element invertible encoding matrix over $\mathbb{F}_2$. Similarly, for an $[n, k]$ QSC, the quantum code space $\mathcal{C}$ is defined as

$$\mathcal{C} = \left\{|\overline{\psi}\rangle = \mathcal{V}\left(|\psi\rangle \otimes |0_{n-k}\rangle\right)\right\} \tag{7}$$

where $\mathcal{V}$ is an n-qubit Clifford transformation[2] and $|\psi\langle\in \mathbb{C}^{2^k}$. The corresponding binary encoding matrix V is a unique $(2n \times 2n)$-element matrix such that for any $\mathcal{P} \in \mathcal{G}_n$, we have [9]

$$[\mathcal{V}\mathcal{P}\mathcal{V}^\dagger] = [\mathcal{P}]V \tag{8}$$

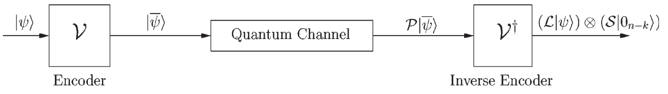

Fig. 1. Quantum transmission model.

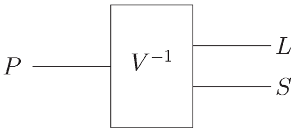

Fig. 2. Circuit representation of the inverse encoder $PV^{-1} = (L : S)$.

where $[\mathcal{P}] = P$, and $[.]$ denotes the effective Pauli group G_n such that $[\mathcal{P}]$ differs from $\mathcal{P}$ by a multiplicative constant, i.e., we have $[\mathcal{P}] = \mathcal{P}/\{\pm 1, \pm i\}$. The rows of V, which are denoted as V_i for $1 \leq i \leq 2n$, are given by $V_i = [\mathcal{V}Z_i\mathcal{V}^\dagger] = [Z_i]V$ for $1 \leq i \leq n$ and $V_i = [\mathcal{V}X_i\mathcal{V}^\dagger] = [X_i]V$ for $n < i \leq 2n$. Here, X_i and Z_i represent the Pauli $\mathbf{X}$ and $\mathbf{Z}$ operators acting on the ith qubit. Furthermore, any codeword in $\mathcal{C}$ is invariant by $\mathcal{V}Z_i\mathcal{V}^\dagger$, for $k < i \leq n$, which therefore corresponds to the stabilizer generators g_i of (3). More explicitly, the rows V_i, for $k < i \leq n$, constitute the $(n-k) \times 2n$ parity-check matrix $\mathbf{H}$ of (4), which meets the symplectic criterion of (5).

At the decoder, the received codeword $|\hat{\psi}\rangle = \mathcal{P}|\overline{\psi}\rangle$ is passed through the inverse encoder $\mathcal{V}^\dagger$, which yields the corrupted transmitted information word $\mathcal{L}|\psi\rangle$ and the associated syndrome $\mathcal{S}|0_{n-k}\rangle$, which is formulated as

$$\begin{aligned}\mathcal{V}^\dagger\mathcal{P}|\overline{\psi}\rangle &= \mathcal{V}^\dagger\mathcal{P}\mathcal{V}\left(|\psi\rangle \otimes |0_{n-k}\rangle\right)\\ &= \left(\mathcal{L}|\psi\rangle\right) \otimes \left(\mathcal{S}|0_{n-k}\rangle\right)\end{aligned} \tag{9}$$

where $\mathcal{L}$ denotes the error imposed on the logical qubits, whereas $\mathcal{S}$ represents the error inflicted on the remaining $(n-k)$ qubits. This transmission process is summarized in Fig. 1.

Since stabilizer codes are analogous to linear block codes, syndrome decoding is employed at the receiver to find the most likely error coset $\mathcal{L}$ given the syndrome $\mathcal{S}$. This is efficiently achieved by exploiting the equivalent binary encoding matrix V of (8), which decomposes the effective n-qubit error imposed on the physical qubits $P = [\mathcal{P}]$ into the effective k-qubit error inflicted on the logical qubits $L = [\mathcal{L}]$ and the corresponding effective $(n-k)$-qubit syndrome $S = [\mathcal{S}]$, as portrayed in Fig. 2, and mathematically represented as

$$PV^{-1} = (L : S). \tag{10}$$

More explicitly, $P \in G_n$, $L \in G_k$, and $S \in G_{n-k}$.

For an $[n, k, m]$ QCC, the encoding matrix V is constructed from repeated use of the seed transformation U shifted by n qubits, as shown in [9, Fig. 6]. More specifically, U is the binary equivalent of an $(n+m)$-qubit symplectic matrix. Furthermore, (10) may be modified as follows [9]:

$$(P_t : M_t)U^{-1} = (M_{t-1} : L_t : S_t) \tag{11}$$

where t and $(t-1)$ denote the current and previous time instants, respectively, whereas M is the effective m-qubit error on the memory states. Furthermore, $2(n-k)$-element binary vector S of (10) and (11) can be decomposed into two

---

[2] Clifford transformation $\mathcal{V}$ is a unitary transformation, which maps an n-qubit Pauli group $\mathcal{G}_n$ onto itself under conjugation [24], i.e.,

$$\mathcal{V}\mathcal{G}_n\mathcal{V}^\dagger = \mathcal{G}_n.$$

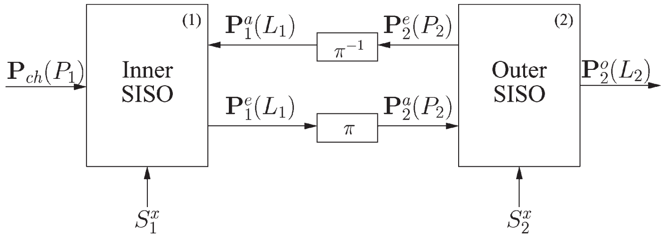

Fig. 3. Schematic of the quantum turbo decoder. $\mathbf{P}_i^a(.)$, $\mathbf{P}_i^e(.)$, and $\mathbf{P}_i^o(.)$ are the *a priori*, extrinsic, and *a posteriori* probabilities related to the ith decoder; P_i and L_i denote the error on the physical and logical qubits, whereas S_i^x represents the syndrome sequence for the ith decoder.

components, yielding $S = S^x + S^z$, where S^x and S^z are the $\mathbf{X}$ and $\mathbf{Z}$ components of syndrome S, respectively. The $(n-k)$-binary error syndrome computed using the parity-check matrix $\mathbf{H}$ only reveals S^x but not S^z [9]. Therefore, those physical errors that only differ in S^z do not have to be differentiated, since they correspond to the same logical error L and can be corrected by the same operations. These are the degenerate errors, which only differ by the stabilizer group, as discussed in Section II-A. Consequently, a quantum turbo decoding algorithm aims at finding the most likely error coset acting on the logical qubits, i.e., L, which satisfies the syndrome S^x.

Similar to the classical turbo codes, quantum turbo decoding invokes an iterative decoding algorithm at the receiver for exchanging *extrinsic* information [11], [25] between the pair of SC soft-in soft-out (SISO) decoders, as shown in Fig. 3. These SISO decoders employ the degenerate decoding approach in [9]. Let P_i and L_i denote the error imposed on the physical and logical qubits, whereas S_i^x represents the syndrome sequence for the ith decoder. Furthermore, $\mathbf{P}_i^a(.)$, $\mathbf{P}_i^e(.)$, and $\mathbf{P}_i^o(.)$ denote the *a priori*, *extrinsic*, and *a posteriori* probabilities [25] related to the ith decoder. Based on this notation, the turbo decoding process can be summarized as follows.

- The inner SISO decoder uses the channel information $\mathbf{P}_{\mathrm{ch}}(P_1)$, the *a priori* information gleaned from the outer decoder $\mathbf{P}_1^a(L_1)$ (initialized to be equiprobable for the first iteration), and the syndrome S_1^x to compute the *extrinsic* information $\mathbf{P}_1^e(L_1)$.
- $\mathbf{P}_1^e(L_1)$ is passed through a quantum interleaver[3] (π) to yield *a priori* information for the outer decoder $\mathbf{P}_2^a(P_2)$.
- Based on the *a priori* information $\mathbf{P}_2^a(P_2)$ and on the syndrome S_2^x, the outer SISO decoder computes both the *a posteriori* information $\mathbf{P}_2^o(L_2)$ and the *extrinsic* information $\mathbf{P}_2^e(P_2)$.
- $\mathbf{P}_2^e(P_2)$ is deinterleaved to obtain $\mathbf{P}_1^a(L_1)$, which is fed back to the inner SISO decoder. This iterative procedure continues until convergence is achieved or the maximum affordable number of iterations is reached.
- Finally, a qubit-based MAP decision is made to determine the most likely error coset L_2.

III. APPLICATION OF EXTRINSIC INFORMATION TRANSFER CHARTS TO QUANTUM TURBO CODES

Here, we will extend the application of EXIT charts to the quantum domain, by appropriately adapting the conventional nonbinary EXIT chart generation technique to the circuit-based quantum syndrome decoding approach. Some of the information presented here might seem redundant to the experts of classical channel coding theory. However, since EXIT charts are not widely known in the quantum community, this introduction was necessary to make this treatise accessible to quantum researchers.

A. *EXIT Charts*

EXIT charts [18], [25], [26] are capable of visualizing the convergence behavior of iterative decoding schemes by exploiting the input/output relations of the constituent decoders in terms of their average mutual information (MI) characteristics. They have been extensively employed for designing near-capacity classical codes [27], [28], [29]. Let us recall that the EXIT chart of an SC scheme visualizes the exchange of the following four MI terms:

- average *a priori* MI of the inner decoder, I_A^1;
- average *a priori* MI of the outer decoder, I_A^2;
- average *extrinsic* MI of the inner decoder, I_E^1;
- average *extrinsic* MI of the outer decoder, I_E^2.

More specifically, I_A^1 and I_E^1 constitute the EXIT curve of the inner decoder, whereas I_A^2 and I_E^2 yield the EXIT curve of the outer decoder. The MI transfer characteristics of both the decoders are plotted in the same graph, with the x- and y-axes of the outer decoder swapped. The resultant EXIT chart quantifies the improvement in the MI as the iterations proceed, which can be viewed as a staircase-shaped decoding trajectory. Having an open tunnel between the two EXIT curves ensures that the decoding trajectory reaches the $(1, y)$ point of perfect convergence.

B. *Quantum-to-Classical Isomorphism*

Before proceeding with the application of EXIT charts for quantum codes, let us elaborate on the quantum-to-classical isomorphism encapsulated in (4), which forms the basis of our EXIT-chart-aided approach. As discussed in Section II-A, a Pauli error operator $\mathcal{P}$ experienced by an N-qubit frame transmitted over a depolarizing channel can be modeled by an effective error vector P, which is a binary vector of length $2N$. The first N bits of P denote Z errors, whereas the remaining N bits represent $\mathbf{X}$ errors, as shown in Fig. 4. More explicitly, an $\mathbf{X}$ error imposed on the first qubit will yield a 0 and a 1 at the first and $(N+1)$th index of P, respectively. Similarly, a $\mathbf{Z}$ error imposed on the first qubit will give a 1 and a 0 at the first and $(N+1)$th index of P, respectively, whereas a Y error on the first qubit will result in a 1 at both the first and $(N+1)$th index of P. Since a depolarizing channel characterized by probability p incurs $\mathbf{X}$, $\mathbf{Y}$ and $\mathbf{Z}$ errors with an equal probability of $p/3$, the effective error vector P reduces to two binary symmetric channels (BSCs) having a crossover probability of $2p/3$, where we have one channel for the $\mathbf{Z}$ errors and the other for the

---

[3] An N-qubit quantum interleaver is an N-qubit symplectic transformation, which randomly permutes the N qubits and applies single-qubit symplectic transformations to the individual qubits [9].

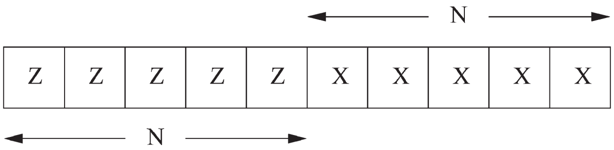

Fig. 4. Effective error (P) corresponding to the error imposed on an N-qubit frame ($\mathcal{P}$).

TABLE I
CORRELATION BETWEEN $\mathbf{X}$ AND $\mathbf{Z}$ ERRORS ON THE iTH QUBIT IN TERMS OF THE CORRESPONDING PROBABILITY OF OCCURRENCE

	$\mathbf{Z}=0$	$\mathbf{Z}=1$
$\mathbf{X}=0$	$1-p$	$p/3$
$\mathbf{X}=1$	$p/3$	$p/3$

$\mathbf{X}$ errors. Hence, a quantum depolarizing channel has been considered analogous to a BSC [22], [30], whose capacity is given by

$$C_{\text{BSC}} = 1 - H_2(2p/3) \tag{12}$$

where H_2 is the binary entropy function. Using (4), we can readily infer that the code rate R_Q of an $[n, k]$ QSC is related to the equivalent classical code rate R_C as follows [22], [31]:

$$R_C = \frac{1}{2}(1 + R_Q). \tag{13}$$

Consequently, the corresponding quantum capacity is as follows [22], [31]:

$$C^Q_{\text{BSC}} = 1 - H_2(2p/3). \tag{14}$$

However, the two BSCs constituting a quantum depolarizing channel are not entirely independent. There is an inherent correlation between the $\mathbf{X}$ and $\mathbf{Z}$ errors [22], which is characterized in Table I. This correlation is taken into account by the turbo decoder in Fig. 3. Alternatively, a quantum depolarization channel can also be considered equivalent to a 4-ary symmetric channel. More explicitly, the ith and the $(N+i)$th index of P constitute the 4-ary symbol. The corresponding classical capacity is equivalent to the maximum rate achievable over each half of the 4-ary symmetric channel, as follows [22], [31]:

$$C_{4-\text{ary}} = \frac{1}{2}\left[2 - H_2(p) - p\log_2(3)\right]. \tag{15}$$

Therefore, using (13), the corresponding quantum capacity can be readily shown to be [22], [31]

$$C^Q_{4-\text{ary}} = 1 - H_2(p) - p\log_2(3) \tag{16}$$

which is known as the hashing bound.[4]

Recall that a quantum code is equivalent to a classical code through (4). More specifically, as mentioned in Section II-A, the decoding of a quantum code is essentially carried out with the aid of the equivalent classical code by exploiting the additional property of degeneracy. Quantum codes employ syndrome decoding [23], which yields information about the *error sequence* rather than the information sequence or coded qubits, hence avoiding the observation of the latter sequences, which would collapse them back to the classical domain.

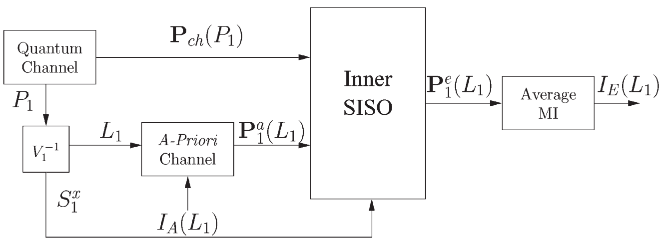

Fig. 5. System model for generating the EXIT chart of the inner decoder.

Since a depolarizing channel is analogous to the BSC and a QTC has an equivalent classical representation, we employ the EXIT chart technique to design near-capacity QTCs. The major difference between the EXIT charts conceived for the classical and quantum domains is that while the former models the *a priori* information concerning the input bits of the inner encoder (and, similarly, the output bits of the outer encoder), the latter models the *a priori* information concerning the corresponding error sequence, i.e., the error sequence related to the input qubits of the inner encoder L_1 (and, similarly, the error sequence related to the output qubits of the outer encoder P_2). This will be dealt with further in the following section.

C. *EXIT Charts for QTCs*

Similar to the classical EXIT charts, in our design, we assume that the interleaver length is sufficiently high to ensure that [18], [25]

- the *a priori* values are fairly uncorrelated;
- the *a priori* information has a Gaussian distribution.

Fig. 5 shows the system model used for generating the EXIT chart of the inner decoder. Here, a quantum depolarizing channel having a depolarizing probability of p generates the error sequence P_1, which is passed through the inverse inner encoder V_1^{-1}. This yields both the error imposed on the logical qubits L_1 and the syndrome S_1^x according to (10). The *a priori* channel block then models the *a priori* information $\mathbf{P}_1^a(L_1)$ such that the average MI between the actual error L_1 and the *a priori* probabilities $\mathbf{P}_1^a(L_1)$ is given by $I_A(L_1)$ [18], [25], [26]. More explicitly, we have $I_A(L_1) = I[L_1, \mathbf{P}_1^a(L_1)]$, where I denotes the average MI function. As discussed in Section III-B, the ith and $(N+i)$th bits of the effective error vector L_1 can be visualized as 4-ary symbols. Consequently, similar to classical nonbinary EXIT charts [32], [33], the *a priori* information is modeled using an independent Gaussian distribution with zero mean and variance σ_A^2, assuming that the $\mathbf{X}$ and $\mathbf{Z}$ errors constituting the 4-ary symbols are independent. Using the channel information $\mathbf{P}_{\text{ch}}(P_1)$, syndrome S_1^x and the *a priori* information, the inner SISO decoder yields the *extrinsic* information $\mathbf{P}_1^e(L_1)$ based on the classic forward–backward recursive coefficients α_t and β_t as follows [9]:

- For a coded sequence of duration N, let $P_1 = [P_{1,1}, P_{1,2}, \ldots, P_{1,t}, \ldots, P_{1,N}]$ and $L_1 = [L_{1,1}, L_{1,2}, \ldots, L_{1,t}, \ldots, L_{1,N}]$, where $P_{1,t} \in G_n$, and $L_{1,t} \in G_k$. More explicitly,

---

[4] The hashing bound determines the code rate at which a random quantum code facilitates reliable transmission for a particular depolarizing probability p [11].

$P_{1,t}=[P_{1,t}^1, P_{1,t}^2, \ldots, P_{1,t}^n]$, and $L_{1,t}=[L_{1,t}^1, L_{1,t}^2, \ldots, L_{1,t}^k]$. For ease of clarification, we will ignore the first subscript, which represents the decoder, in the algorithm given below, i.e., we have $P_1 = P$ and $L_1 = L$. Similarly, $S_1^x = S^x$.

- Let $U = (U_P : U_M)$ so that U_P is the binary matrix formed by the first $2n$ columns of U of (11), whereas U_M is the binary matrix formed by the last $2m$ columns of U. Therefore, we have

$$P_t = (M_{t-1} : L_t : S_t)U_P \tag{17}$$

$$M_t = (M_{t-1} : L_t : S_t)U_M. \tag{18}$$

- Let $\alpha_t(M_t)$ be the forward recursive coefficient, which is defined as follows:

$$\begin{aligned}\alpha_t(M_t) &\triangleq \mathbf{P}\left(M_t|S_{\leq t}^x\right)\\ &\propto \sum_{\mu,\lambda,\sigma} \mathbf{P}^a(L_t = \lambda)\mathbf{P}_{\mathrm{ch}}(P_t)\alpha_{t-1}(\mu)\end{aligned} \tag{19}$$

where $\mu \in G_m$, $\lambda \in G_k$ and $\sigma \in G_{n-k}$, while $\sigma = \sigma_x + \sigma_z$, having $\sigma_x = S_t^x$. Furthermore, we have $P_t = (\mu : \lambda : \sigma)U_P$ and $M_t = (\mu : \lambda : \sigma)U_M$. The channel information $\mathbf{P}_{\mathrm{ch}}(P_t)$ is computed assuming that each qubit is independently transmitted over a quantum depolarizing channel having a depolarizing probability of p, whose channel transition probabilities are given by [9]

$$\mathbf{P}_{\mathrm{ch}}\left(P_t^i\right) = \begin{cases} 1-p, & \text{if } \mathcal{P}_t^i = \mathbf{I} \\ p/3, & \text{if } \mathcal{P}_t^i \in \{\mathbf{X}, \mathbf{Z}, \mathbf{Y}\}. \end{cases} \tag{20}$$

- Let $\beta_t(M_t)$ be the backward recursive coefficient, which is defined as follows:

$$\begin{aligned}\beta_t(M_t) &\triangleq \mathbf{P}\left(M_t|S_{>t}^x\right)\\ &\propto \sum_{\lambda,\sigma} \mathbf{P}^a(L_t = \lambda)\mathbf{P}_{\mathrm{ch}}(P_{t+1})\beta_{t+1}(M_{t+1})\end{aligned} \tag{21}$$

where $P_{t+1} = (M_t : \lambda : \sigma)U_P$, and $M_{t+1} = (M_t : \lambda : \sigma)U_M$.

- Finally, we have the *a posteriori* probability $\mathbf{P}^o(L_t)$, which is given by

$$\begin{aligned}\mathbf{P}^o(L_t) &\triangleq \mathbf{P}(L_t|S^x)\\ &\propto \sum_{\mu,\sigma} \mathbf{P}^a(L_t)\mathbf{P}_{\mathrm{ch}}(P_t)\alpha_{t-1}(\mu)\beta_t(M_t)\end{aligned} \tag{22}$$

where $P_t = (\mu : L_t : \sigma)U_P$ and $M_t = (\mu : L_t : \sigma)U_M$.

- Marginalized probabilities $\mathbf{P}^o(L_t^j)$ for $j \in \{0, k-1\}$ are then computed from $\mathbf{P}^o(L_t^j)$, and the *a priori* information is removed to yield the *extrinsic* probabilities [11], i.e., we have

$$\ln\left[\mathbf{P}^e\left(L_t^j\right)\right] = \ln\left[\mathbf{P}^o\left(L_t^j\right)\right] - \ln\left[\mathbf{P}^a\left(L_t^j\right)\right]. \tag{23}$$

Finally, the *extrinsic* average MI between L_1 and $\mathbf{P}_1^e(L_1)$ is computed, i.e., $I_E(L_1) = I[L_1, \mathbf{P}_1^e(L_1)]$. Since the equivalent classical capacity of a quantum channel is given by the capacity achievable over each half of the 4-ary symmetric channel as depicted in (15), $I_E(L_1)$ is the normalized MI of the 4-ary symbols, which can be computed based on [33] and [34] as

$$I_E(L_1) = \frac{1}{2}\left(2 + \mathrm{E}\left[\sum_{\mathrm{m}=0}^{3} \mathbf{P}_1^e\left(L_1^{j(\mathrm{m})}\right)\log_2 \mathbf{P}_1^e\left(L_1^{j(\mathrm{m})}\right)\right]\right) \tag{24}$$

where E is the expectation (or time average) operator, and $L_1^{j(\mathrm{m})}$ is the 4-ary mth hypothetical error imposed on the logical qubits. More explicitly, since the error on each qubit is represented by an equivalent pair of classical bits, $L_1^{j(\mathrm{m})}$ is a 4-ary classical symbol with $\mathrm{m} \in \{0, 3\}$. The process is repeated for a range of $I_A(L_1) \in [0, 1]$ values for obtaining the *extrinsic* information transfer characteristics at the depolarizing probability p. The resultant inner EXIT function T_1 of the specific inner decoder may be defined as follows:

$$I_E(L_1) = T_1\left[I_A(L_1), p\right] \tag{25}$$

which is dependent on the depolarizing probability p of the quantum channel.

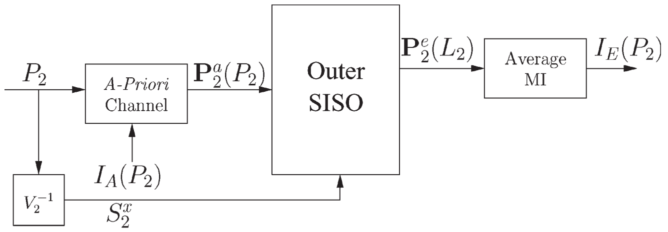

Fig. 6. System model for generating the EXIT chart of the outer decoder.

The system model used for generating the EXIT chart of the outer decoder is shown in Fig. 6. As inferred from the figure, the EXIT curve of the outer decoder is independent of the channel's output information. The *a priori* information is generated by the *a priori* channel based on P_2 (error on the physical qubits of the second decoder) and $I_A(P_2)$, which is the average MI between P_2 and $\mathbf{P}_2^a(P_2)$. Furthermore, as for the inner decoder, P_2 is passed through the inverse outer encoder V_2^{-1} to compute S_2^x, which is fed to the outer SISO decoder to yield the *extrinsic* information $\mathbf{P}_2^e(P_2)$. Based on (19) and (21), this may be formulated as follows [9]:

$$\begin{aligned}\mathbf{P}^o(P_t) &\triangleq \mathbf{P}(P_t|S^x)\\ &\propto \sum_{\mu,\lambda,\sigma} \mathbf{P}(P_t)\mathbf{P}(L_t = \lambda)\alpha_{t-1}(\mu)\beta_t(M_t)\end{aligned} \tag{26}$$

where $P_t = (\mu : \lambda : \sigma)U_P$, and $M_t = (\mu : \lambda : \sigma)U_M$. The resultant probabilities are marginalized, and the *a priori* information is removed similar to (23). The average MI between P_2 and $\mathbf{P}_2^e(P_2)$ is then calculated using (24). The resultant EXIT chart is characterized by the following MI transfer function:

$$I_E(P_2) = T_2\left[I_A(P_2)\right] \tag{27}$$

where T_2 is the outer EXIT function, which is dependent on the specific outer decoder but is independent of the depolarizing probability p.

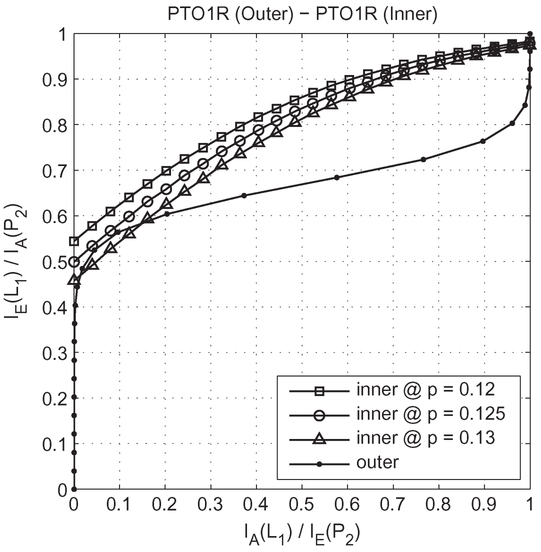

Fig. 7. EXIT curves of a QTC parametrized by the increasing depolarizing probability p. Rate-1/9 QTC having PTO1R as both the inner and outer components was used.

Finally, the MI transfer characteristics of both decoders characterized by (25) and (27) are plotted in the same graph, with the x- and y-axes of the outer decoder swapped.

IV. RESULTS AND DISCUSSIONS

A. Accuracy of EXIT Chart Predictions

To verify the accuracy of our EXIT-chart-based approach, we have analyzed the convergence behavior of a rate-1/9 QTC, consisting of two identical rate-1/3 QCCs. More specifically, for both the inner and outer decoders, we have used the configuration termed as "PTO1R" in [10] and [11], which is a noncatastrophic but quasi-recursive code.

Our first aim was to predict the convergence threshold using EXIT charts, which would otherwise require time-consuming word error rate/qubit error rate (WER/QBER) simulations. The convergence threshold can be determined by finding the maximum depolarizing probability p, which yields a marginally open EXIT tunnel between the EXIT curves of the inner and outer decoders, hence facilitating an infinitesimally low QBER. Fig. 7 shows the EXIT curves for the inner and outer decoders, where the area under the EXIT curve of the inner decoder decreases upon increasing p. Eventually, the inner and outer curves cross over, when p is increased to $p = 0.13$. More explicitly, increasing p beyond 0.125 closes the EXIT tunnel. Hence, the convergence threshold is around $p = 0.125$.

Fig. 8 shows two decoding trajectories superimposed on the EXIT chart in Fig. 7 at $p = 0.125$. We have used a 30 000-qubit long interleaver. As shown in Fig. 8, the trajectory successfully reaches the $(x, y) = (1, y)$ point of the EXIT chart. This, in turn, guarantees an infinitesimally low QBER at $p = 0.125$ for an interleaver of infinite length.

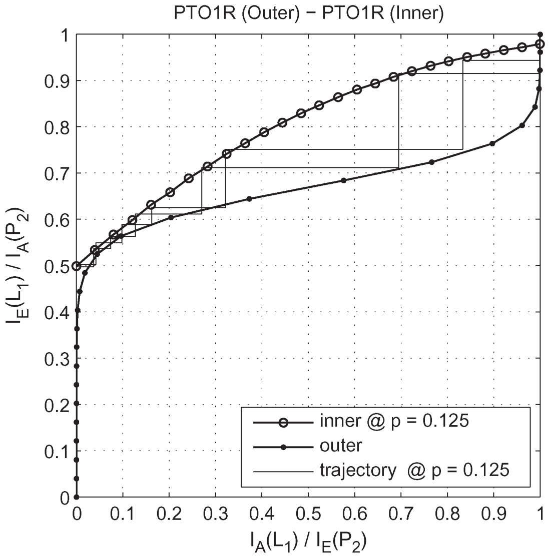

Fig. 8. EXIT chart of a QTC with decoding trajectories at $p = 0.125$. Rate-1/9 QTC having PTO1R as both the inner and outer components with an interleaver length of 30 000 qubits was used.

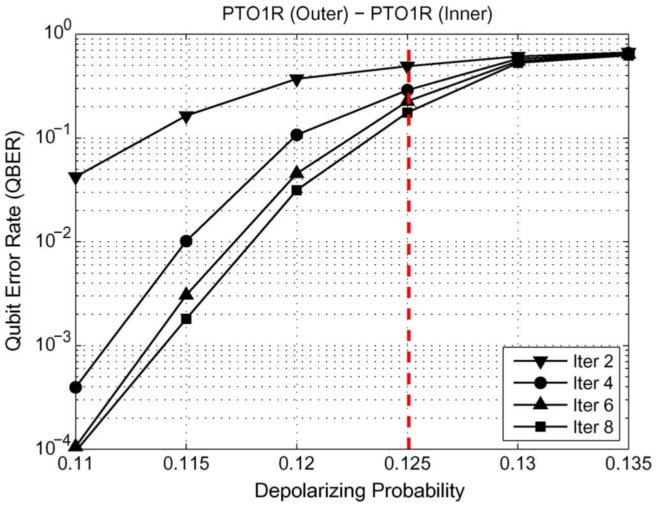

Fig. 9. QBER performance curve with an increasing iteration number for an interleaver length of 3000 qubits. Rate-1/9 QTC having PTO1R as both the inner and outer components was used.

We have further verified the validity of our EXIT chart predictions using QBER simulations. Fig. 9 shows the QBER performance curve for an interleaver length of 3000 qubits. The performance improves upon increasing the number of iterations. More specifically, the turbo-cliff region starts around $p = 0.125$, whereby the QBER drops as the iterations proceed. Therefore, our EXIT chart predictions closely follow the Monte Carlo simulation results.

B. Entanglement-Assisted and Unassisted Inner Codes

All noncatastrophic convolutional codes are nonrecursive [9]. Therefore, the resultant families of QTCs have a bounded minimum distance and do not have a true iterative threshold. To circumvent this limitation of QTCs, Wilde *et al.* [10], [11] proposed to employ entanglement-assisted inner codes, which are recursive and noncatastrophic. The resulting families of entanglement-assisted QTCs have an unbounded minimum distance [10], [11], i.e., their minimum distance increases almost linearly with the interleaver length. Here, we verify this by analyzing the inner decoder's EXIT curves for both the unassisted

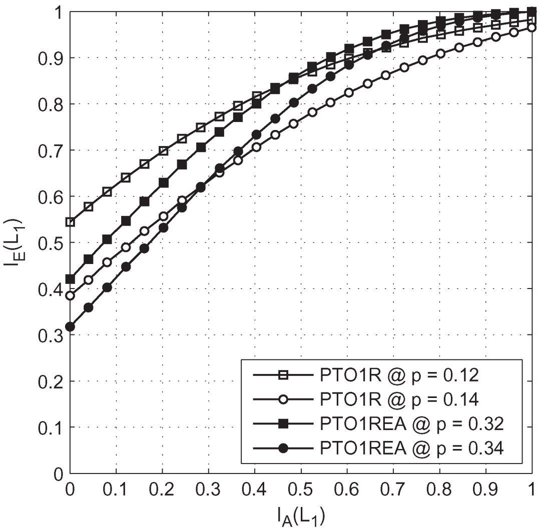

Fig. 10. Comparison of the inner EXIT curves of both unassisted and entanglement-assisted QCCs, which are labeled as PTO1R and PTO1REA, respectively.

(nonrecursive) and entanglement-assisted (recursive) inner convolutional codes.

For classical recursive inner codes, the inner decoder's EXIT curve reaches the $(x, y) = (1, 1)$ point,[5] which guarantees perfect decoding convergence to a vanishingly low QBER as well as having an unbounded minimum distance for the infinite family of QTCs [9] based on these inner codes. Consequently, the resulting families of QTCs have unbounded minimum distance, and hence, an arbitrarily low QBER can be achieved for an infinitely long interleaver. This also holds true for recursive QCCs, as shown in Fig. 10. In this figure, we compare the inner decoder's EXIT curves of both the unassisted and the entanglement-assisted QCCs in [10], which are labeled "PTO1R" and "PTO1REA," respectively. For the PTO1R configuration, decreasing the depolarizing probability from $p = 0.14$ to $p = 0.12$ shifts the inner decoder's EXIT curve upward and toward the (1,1) point. Hence, the EXIT curve will manage to reach the (1,1) point only at very low values of depolarizing probability. By contrast, the EXIT curve of PTO1REA always terminates at (1,1), regardless of the value of p. Therefore, provided that an open EXIT tunnel exists and the interleaver length is sufficiently long, the decoding trajectories of an entanglement-assisted QTC will always reach the (1,1) point, thus guaranteeing an arbitrarily low QBER for the infinite family of QTCs based on these inner codes. In other words, the performance improves upon increasing the interleaver length, thus implying that the minimum distance increases upon increasing the interleaver length, and therefore, the resultant QTCs have an unbounded minimum distance.

C. Optimized QTC Design

The QTC design in [10] and [11] characterized in Fig. 8 exhibits a large area between the inner and outer decoder's EXIT curves. The larger the "open-tunnel" area, the farther the QBER performance curve from the achievable capacity limit [25]. Consequently, various distance-spectra-based QTCs investigated in [11] operate within 0.9 dB of the hashing bound. For the sake of achieving a near-capacity performance, we minimize the area between the inner and outer EXIT curves, so that a narrow but still marginally open tunnel exists at the highest possible depolarizing probability. Our aim was to construct a rate-1/9 QTC relying on an entanglement-assisted inner code (recursive and noncatastrophic) and an unassisted outer code (noncatastrophic) having a memory of 3 and a rate of 1/3. The resultant QTC has an entanglement consumption rate of 6/9, for which the corresponding maximum tolerable depolarizing probability was shown to be $p_{\max} = 0.3779$ in [11].

For the sake of designing a near-capacity QTC operating close to the capacity limit of $p_{\max} = 0.3779$, we randomly selected both inner and outer encoders from the Clifford group according to the algorithm in [35] to find the inner and outer components, which minimize the area between the corresponding EXIT curves. Based on this design criterion, we found an optimal inner and outer code pair whose seed transforms[6] (decimal representation) are given by

$$\begin{aligned} U_{\text{inner}} = \{&4091, 3736, 2097, 1336, 1601, 279 \\ &3093, 502, 1792, 3020, 226, 1100\} \qquad (28) \\ U_{\text{outer}} = \{&1048, 3872, 3485, 2054, 983, 3164 \\ &3145, 1824, 987, 3282, 2505, 1984\}. \qquad (29) \end{aligned}$$

Fig. 11 shows the corresponding EXIT chart at the convergence threshold of $p = 0.35$. As observed in Fig. 11, a marginally open EXIT tunnel exists between the two curves, which facilitates for the decoding trajectories to reach the (1,1) point. Hence, our optimized QTC has a convergence threshold of $p = 0.35$, which is only $[10 \times \log_{10}(0.35/0.3779)] = 0.3$ dB from the maximum tolerable depolarizing probability of 0.3779. The corresponding QBER performance curves recorded for our optimized design are given in Fig. 12. A maximum of 15 iterations were used, while the interleaver length was increased from 1500 to 12 000. Similar to classical turbo codes, increasing the interleaver length for $p < 0.35$ improves the attainable performance. Furthermore, Fig. 12 also compares our optimized design with the rate-1/9 QTC in [11] for an interleaver length of 3000, which is labeled "PTO1REA-PTO1R" in the figure. For the "PTO1REA-PTO1R" configuration, the turbo-cliff region emerges around 0.31, which is within 0.9 dB of the capacity limit. Therefore, our EXIT-chart-based QTC outperforms the QTC design based on the distance spectrum [11]. More specifically, the "PTO1REA-PTO1R" configuration yields a QBER of 10^{-3} at $p = 0.2925$, whereas our optimized QTC gives a

---

[5] Note that we only need $(x, y) = (1, y)$ to achieve decoding convergence to an infinitesimally low QBER. However, this requires an outer code having a sufficiently large minimum distance for the sake of ensuring that the outer code's EXIT curve does not intersect with that of the inner code before reaching the $(1, y)$ point. Unfortunately, an outer code having a large minimum distance would result in an EXIT curve having a large open-tunnel area. Thus, it will operate far from the capacity.

[6] See [11] for the details of this representation.

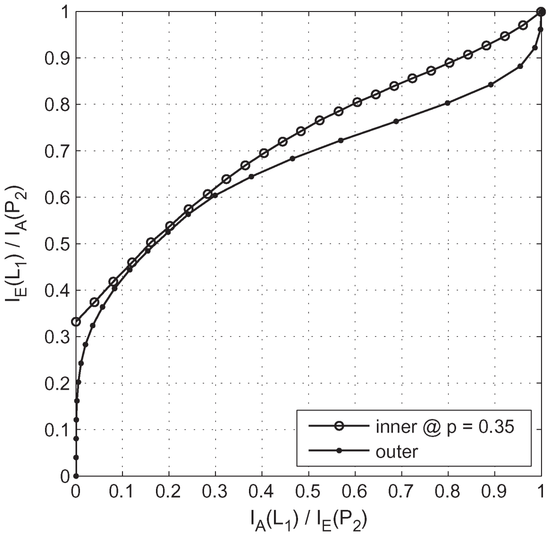

Fig. 11. EXIT chart of the optimized rate-1/9 QTC (Interleaver length = 30 000 qubits).

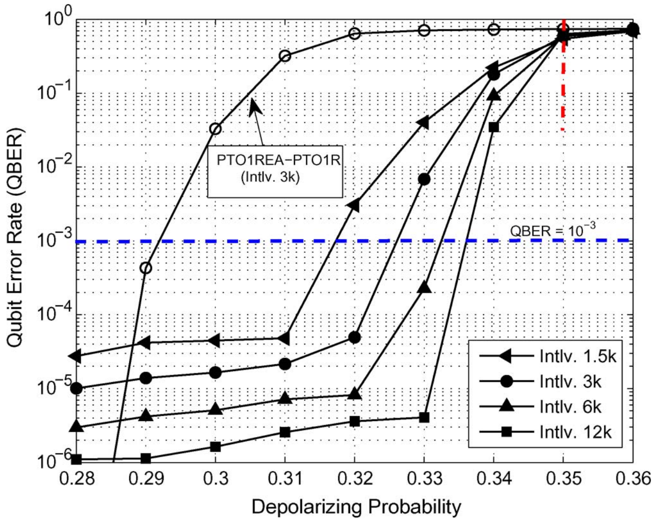

Fig. 12. QBER performance curves of the optimized rate-1/9 QTC for varying interleaver lengths and a maximum of 15 iterations.

QBER of 10^{-3} at $p = 0.3275$. Hence, our optimized QTC outperforms the "PTO1REA-PTO1R" configuration by about $[10 \times \log_{10}(0.2925/0.3275)] = 0.5$ dB at a QBER of 10^{-3}. However, our main design objective was to not carry out an exhaustive code search but to demonstrate the explicit benefit of our EXIT-chart-based approach in the context of quantum codes. It must also be observed in Fig. 12 that a relatively high error floor exists for our optimized design, which is gradually reduced upon increasing the interleaver length. This is because the outer code has a low minimum distance of only 3. Its truncated distance spectrum is as follows:

$$\begin{aligned} D(x) =\, & 2x^3 + 19x^4 + 108x^5 + 530x^6 + 2882x^7 + 14179x^8 \\ & + 62288x^9 + 243234x^{10} + 845863x^{11} + 1165784x^{12} \\ & + 2501507x^{13} + 744394x^{14}. \end{aligned}$$

By contrast, the truncated distance spectrum of "PTO1R," which has a minimum distance of 5, is given by [11]

$$\begin{aligned} D(x) = 11x^5 + 47x^6 + 253x^7 + 1187x^8 + 6024x^9 \\ +30529x^{10} + 153051x^{11} + 771650x^{12}. \end{aligned}$$

Consequently, as gleaned from Fig. 12, the "PTO1REA-PTO1R" configuration has a much lower error floor ($< 10^{-6}$), since the outer code "PTO1R" has a higher minimum distance. However, this enlarges the area between the inner and outer decoder's EXIT curves, thus driving the performance farther away from the achievable capacity, as shown in Fig. 8. Hence, there is a tradeoff between the minimization of the error floor and achieving a near-capacity performance. More specifically, while the distance-spectrum-based design primarily aims at achieving a lower error floor, the EXIT-chart-based design strives for achieving a near-capacity performance.

V. CONCLUSION

In this paper, we have extended the application of classical nonbinary EXIT charts to the circuit-based syndrome decoder of QTCs, to facilitate the EXIT-chart-based design of QTCs. We have verified the accuracy of our EXIT chart generation approach by comparing the convergence threshold predicted by the EXIT chart to the Monte Carlo simulation results. Furthermore, we have shown with the aid of EXIT charts that entanglement-assisted recursive QCCs have an unbounded minimum distance. Moreover, we have designed an optimal entanglement-assisted QTC using EXIT charts, which outperforms the distance-spectra-based QTC in [11] by about 0.5 dB at a QBER of 10^{-3}.

ACKNOWLEDGMENT

The authors would like to thank Dr. M. M. Wilde for the valuable discussions and the anonymous reviewers for their insightful advice and comments.

REFERENCES

[1] S. X. Ng and L. Hanzo, "On the MIMO channel capacity of multidimensional signal sets," *IEEE Trans. Veh. Technol.*, vol. 55, no. 2, pp. 528–536, Mar. 2006.

[2] J.-M. Chung, J. Kim, and D. Han, "Multihop hybrid virtual MIMO scheme for wireless sensor networks," *IEEE Trans. Veh. Technol.*, vol. 61, no. 9, pp. 4069–4078, Nov. 2012.

[3] J. Lee and S.-H. Lee, "A compressed analog feedback strategy for spatially correlated massive MIMO systems," in *Proc. IEEE VTC Fall*, 2012, pp. 1–6.

[4] S. Imre and F. Balazs, *Quantum Computing and Communications: An Engineering Approach*. Hoboken, NJ, USA: Wiley, 2005.

[5] P. Botsinis, S. X. Ng, and L. Hanzo (2013). Quantum search algorithms, quantum wireless, a low-complexity maximum likelihood iterative quantum multi-user detector design. *IEEE Access* [Online]. vol. 1, pp. 94–122. Available: http://ieeexplore.ieee.org/xpl/articleDetails.jsp?arnumber=6515077

[6] M. A. Nielsen and I. L. Chuang, *Quantum Computation and Quantum Information*. Cambridge, U.K.: Cambridge Univ. Press, 2000.

[7] X. Zhou and M. McKay, "Secure transmission with artificial noise over fading channels: Achievable rate and optimal power allocation," *IEEE Trans. Veh. Technol.*, vol. 59, no. 8, pp. 3831–3842, Oct. 2010.

[8] D. Poulin, J.-P. Tillich, and H. Ollivier, "Quantum serial turbo-codes," in *Proc. IEEE ISIT*, Jul. 2008, pp. 310–314.

[9] D. Poulin, J. Tillich, and H. Ollivier, "Quantum serial turbo codes," *IEEE Trans. Inf. Theory*, vol. 55, no. 6, pp. 2776–2798, Jun. 2009.

[10] M. M. Wilde and M.-H. Hsieh, “Entanglement boosts quantum turbo codes,” in *Proc. IEEE ISIT*, Aug. 2011, pp. 445–449.

[11] M. Wilde, M.-H. Hsieh, and Z. Babar, “Entanglement-assisted quantum turbo codes,” *IEEE Trans. Inf. Theory*, vol. 60, no. 2, pp. 1203–1222, Feb. 2014.

[12] Z. Babar, S. X. Ng, and L. Hanzo, “Near-capacity code design for entanglement-assisted classical communication over quantum depolarizing channels,” *IEEE Trans. Commun.*, vol. 61, no. 12, pp. 4801–4807, Dec. 2013.

[13] H. Ollivier and J.-P. Tillich (2003, Oct.). Description of a quantum convolutional code. *Phys. Rev. Lett.* [Online]. vol. 91, no. 17, pp. 177 902-1–177 902-4. Available: http://link.aps.org/doi/10.1103/PhysRevLett.91.177902

[14] quant-ph/0401134 H. Ollivier and J. P. Tillich, Quantum Convolutional Codes: Fundamentals 2004, quant-ph/0401134.

[15] G. D. Forney, M. Grassl, and S. Guha, “Convolutional and tail-biting quantum error-correcting codes,” *IEEE Trans. Inf. Theory*, vol. 53, no. 3, pp. 865–880, Mar. 2007.

[16] M. Grassl and M. Rotteler, “Constructions of quantum convolutional codes,” in *Proc. IEEE ISIT*, Jun. 2007, pp. 816–820.

[17] M. Houshmand and M. Wilde, “Recursive quantum convolutional encoders are catastrophic: A simple proof,” *IEEE Trans. Inf. Theory*, vol. 59, no. 10, pp. 6724–6731, Oct. 2013.

[18] S. ten Brink, “Convergence behavior of iteratively decoded parallel concatenated codes,” *IEEE Trans. Commun.*, vol. 49, no. 10, pp. 1727–1737, Oct. 2001.

[19] D. Gottesman, “Class of quantum error-correcting codes saturating the quantum Hamming bound,” *Phys. Rev. A, At. Mol. Opt. Phys.*, vol. 54, no. 3, pp. 1862–1868, Sep. 1996.

[20] E. Pelchat and D. Poulin, “Degenerate Viterbi decoding,” *IEEE Trans. Inf. Theory*, vol. 59, no. 6, pp. 3915–3921, Jun. 2013.

[21] R. Cleve (1997, Jun.). Quantum stabilizer codes and classical linear codes. *Phys. Rev. A, At. Mol. Opt. Phys.* [Online]. vol. 55, no. 6, pp. 4054–4059. Available: http://link.aps.org/doi/10.1103/PhysRevA.55.4054

[22] D. J. C. Mackay, G. Mitchison, and P. L. Mcfadden, “Sparse-graph codes for quantum error-correction,” *IEEE Trans. Inf. Theory*, vol. 50, no. 10, pp. 2315–2330, Oct. 2003.

[23] Z. Babar, S. X. Ng, and L. Hanzo, “Reduced-complexity syndrome-based TTCM decoding,” *IEEE Commun. Lett.*, vol. 17, no. 6, pp. 1220–1223, Jun. 2013.

[24] J. Dehaene and B. De Moor (2003, Oct.). Clifford group, stabilizer states, linear and quadratic operations over GF(2). *Phys. Rev. A, At. Mo. Opt. Phys.* [Online]. vol. 68, no. 4, pp. 042318-1–042318-10. Available: http://link.aps.org/doi/10.1103/PhysRevA.68.042318

[25] L. Hanzo, T. H. Liew, B. L. Yeap, R. Y. S. Tee, and S. X. Ng, *Turbo Coding, Turbo Equalisation and Space–Time Coding: EXIT-Chart-Aided Near-Capacity Designs for Wireless Channels*, 2nd ed. New York, NY, USA: Wiley, Mar. 2011.

[26] M. El-Hajjar and L. Hanzo, “EXIT charts for system design and analysis,” *IEEE Commun. Surveys Tuts.*, vol. 16, no. 1, pp. 1–27, May 2013.

[27] S. Ten Brink, “Rate one-half code for approaching the Shannon limit by 0.1 dB,” *Electron. Lett.*, vol. 36, no. 15, pp. 1293–1294, Jul. 2000.

[28] L. Kong, S. X. Ng, R. Maunder, and L. Hanzo, “Maximum-throughput irregular distributed space–time code for near-capacity cooperative communications,” *IEEE Trans. Veh. Technol.*, vol. 59, no. 3, pp. 1511–1517, Mar. 2010.

[29] S. Ibi, T. Matsumoto, R. Thoma, S. Sampei, and N. Morinaga, “EXIT chart-aided adaptive coding for multilevel BICM with turbo equalization in frequency-selective MIMO channels,” *IEEE Trans. Veh. Technol.*, vol. 56, no. 6, pp. 3757–3769, Nov. 2007.

[30] M. M. Wilde, *Quantum Information Theory*. Cambridge, USA: Cambridge Univ. Press, May 2013. [Online]. Available: http://arxiv.org/abs/1106.1445

[31] P. Tan and J. Li, “Efficient quantum stabilizer codes: LDPC and LDPC-convolutional constructions,” *IEEE Trans. Inf. Theory*, vol. 56, no. 1, pp. 476–491, Jan. 2010.

[32] A. Grant, “Convergence of non-binary iterative decoding,” in *Proc. IEEE Global Telecommun. Conf.*, 2001, vol. 2, pp. 1058–1062.

[33] J. Kliewer, S. X. Ng, and L. Hanzo, “Efficient computation of EXIT functions for non-binary iterative decoding,” *IEEE Trans. Commun.*, vol. 54, no. 12, pp. 2133–2136, Dec. 2006.

[34] S. X. Ng, O. Alamri, Y. Li, J. Kliewer, and L. Hanzo, “Near-capacity turbo trellis coded modulation design based on EXIT charts and union bounds,” *IEEE Trans. Commun.*, vol. 56, no. 12, pp. 2030–2039, Dec. 2008.

[35] D. P. Divincenzo, D. Leung, and B. Terhal, “Quantum data hiding,” *IEEE Trans. Inf. Theory*, vol. 48, no. 3, pp. 580–598, Mar. 2002.

Zunaira Babar received the B.Eng. degree in electrical engineering from the National University of Science and Technology, Islamabad, Pakistan, in 2008 and the M.Sc. degree (with distinction) in wireless communications from the University of Southampton, Southampton, U.K., in 2011, where she is currently working toward the Ph.D. degree with the Communications, Signal Processing, and Control Group, School of Electronics and Computer Science.

Her research interests include quantum error correction codes, channel coding, coded modulation, iterative detection, and cooperative communications.

Soon Xin Ng (S’99–M’03–SM’08) received the B.Eng. degree (first-class honors) in electronics engineering and the Ph.D. degree in wireless communications from the University of Southampton, Southampton, U.K., in 1999 and 2002, respectively.

From 2003 to 2006, he was a Postdoctoral Research Fellow working on collaborative European research projects known as SCOUT, NEWCOM, and PHOENIX. Since August 2006, he has been a member of the academic staff with the School of Electronics and Computer Science, University of Southampton. He is involved in the OPTIMIX and CONCERTO European projects, as well as the IU-ATC and UC4G projects. He is currently a Senior Lecturer with the University of Southampton. He has published over 170 papers and coauthored two John Wiley/IEEE Press books in his areas of interest. His research interests include adaptive coded modulation, coded modulation, channel coding, space–time coding, joint source and channel coding, iterative detection, orthogonal frequency-division multiplexing, multiple-input multiple-output, cooperative communications, distributed coding, quantum error correction codes, and joint wireless-and-optical-fiber communications.

Dr. Ng is a Chartered Engineer and a Fellow of the Higher Education Academy in the United Kingdom.

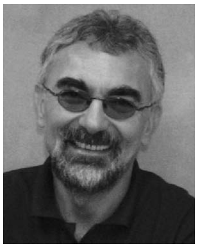

Lajos Hanzo (M’91–SM’92–F’04) received the M.S. degree in electronics and the Ph.D. degree from Budapest University of Technology and Economics (formerly, Technical University of Budapest), Budapest, Hungary, in 1976 and 1983, respectively; the D.Sc. degree from the University of Southampton, Southampton, U.K., in 2004; and the “Doctor Honoris Causa” degree from Budapest University of Technology and Economics in 2009.

During his 38-year career in telecommunications, he has held various research and academic posts in Hungary, Germany, and the U.K. Since 1986, he has been with the School of Electronics and Computer Science, University of Southampton, where he holds the Chair in Telecommunications. He is currently directing a 100-strong academic research team, working on a range of research projects in the field of wireless multimedia communications sponsored by industry, the Engineering and Physical Sciences Research Council of U.K., the European Research Council’s Advanced Fellow Grant, and the Royal Society Wolfson Research Merit Award. During 2008–2012, he was a Chaired Professor with Tsinghua University, Beijing, China. He is an enthusiastic supporter of industrial and academic liaison and offers a range of industrial courses. He has successfully supervised more than 80 Ph.D. students, coauthored 20 John Wiley/IEEE Press books on mobile radio communications totaling in excess of 10 000 pages, published more than 1400 research entries on IEEE Xplore, and presented keynote lectures. He has more than 19 000 citations. His research is funded by the European Research Council’s Senior Research Fellow Grant. For further information on research in progress and associated publications, see http://www-mobile.ecs.soton.ac.uk.

Dr. Hanzo is a Fellow of the Royal Academy of Engineering, The Institution of Engineering and Technology, and the European Association for Signal Processing. He is also a Governor of the IEEE Vehicular Technology Society. He has served as the Technical Program Committee Chair and the General Chair of IEEE conferences, has presented keynote lectures, and has been awarded a number of distinctions. During 2008–2012, he was the Editor-in-Chief of the IEEE Press.